Recrystallized hard zone and resultant tri-modal microstructure produces superior mechanical properties in a single-phase heterostructured high-entropy alloy

Shu-Yi Tung [a], Ting-En Hsu [a], Yuntian Zhu [b], Ming-Hung Tsai [a,c,*]

[a] *Department of Materials Science and Engineering, National Chung Hsing University, Taichung, Taiwan*
[b] *Department of Materials Science and Engineering, City University of Hong Kong, Kowloon, Hong Kong, PR China*
[c] *High-Entropy Materials Center, National Tsing Hua University, Hsinchu, Taiwan*

ABSTRACT

Heterostructured high-entropy alloys (HS-HEAs) integrate two innovative concepts in metallic materials that encompass alloy design and microstructural engineering. HS-HEAs have demonstrated outstanding mechanical properties. However, it remains challenging to explore these materials due to the intricate nature of their composition and microstructure. In this study, we introduced heterostructures into a single-phase FCC HEA through cold rolling and partial recrystallization. This process resulted in an exceptionally high density of nanoscale recrystallization twins, leading to significant hardening and the formation of heterogeneous hard zones in recrystallized regions with small grain sizes. This tri-modal heterostructure results in improved balance between strength and ductility, high zone boundary density and strong hetero-deformation induced (HDI) effects, and a unique two-stage strain partitioning mechanism that postpones necking. As a result, the alloy exhibits enhanced strength and ductility, resulting in superior mechanical properties. The identification of the recrystallized hard zones is crucial for gaining a proper understanding of the hetero-zones in HEAs and provides valuable insights for the future design of HS-HEAs.

1. Introduction

High- and medium-entropy alloys (HEAs and MEAs) have attracted extensive attention of the materials community in the past two decades [1–4]. An intriguing phenomenon in these materials is that despite comprising many different elements, they can often form simple solid solution phases. In fact, these solid solution phases can exhibit extraordinary properties. For instance, CoCrNi and CoCrFeMnNi showcase exceptional fracture toughness both in ambient and cryogenic environments [5–11]. However, these FCC solid solutions have only modest yield strength. Hence, numerous efforts have been made to boost their strength by refining their microstructure. However, the outcomes have proven rather modest. For instance, in the case of CoCrNi with a grain size of 1.26 μm, the yield strength (YS) is only 400 MPa [12]. Nanocrystalline HEAs obtained through severe plastic deformation can elevate the yield strength to the GPa level, but they are accompanied by limited sample sizes and a significant reduction in ductility [12–14]. Traditional strengthening approaches are not quite effective in avoiding

the trade-off between strength and ductility.

A novel concept called heterostructured materials (HSMs) seems quite promising [15–17]. HSMs are materials that contain zones with significant differences in strength, but the sizes and geometries of these distinct regions can vary notably. Such heterogeneity, can lead to hetero-deformation induced strengthening and hetero-deformation induced strain hardening near the boundary of the hetero-zones [18, 19]. The former enhances the strength while the latter improves the ductility of the material, leading to better overall properties. Such beneficial effects, of course, require proper engineering of the morphology and the relative volume fraction of the hetero-zones. It has been proposed that the ideal microstructure for HSMs would be one with 20–30 % volume fraction of soft lamella embedded in a hard matrix since this would maximize the hetero-deformation induced strengthening effects [17,20]. This has been demonstrated by Wu et al., who subjected pure titanium to cold rolling followed by partial recrystallization annealing, yielding a heterogeneous lamellar structure. This unique microstructure displays strength equivalent to the

---

* Corresponding author.
  E-mail address: mhtsai@nchu.edu.tw (M.-H. Tsai).

ultrafine-grained Ti while retaining uniform elongation similar to coarse-grained Ti [16].

It is, therefore, logical to combine the two important trends – the unique composition design in HEAs and the distinct microstructure engineering in heterostructured materials, to fabricate heterostructured HEAs, or HS-HEAs, that could harvest the advantages from both ideas and obtain even better properties [21–29]. Indeed, Du et al. prepared dual heterogeneous nanostructures composed of partially recrystallized structure and heterogeneous $L1_2$ precipitates through deliberately designed compositions and processing methods, resulting in an ultimate tensile strength of 2.2 GPa and a uniform elongation of 13 % [27]. This represents a highly successful design of heterogeneous high-entropy alloys. Besides precipitation hardened HEAs, heterostructure design has also been extended to eutectic high-entropy alloys [29–32]. By controlling the hierarchical heterostructure and grain size, different types of deformation twins can be triggered to enhance the strain hardening capability, thereby improving the mechanical properties of eutectic high-entropy alloys [28]. Compared to as-cast eutectic high-entropy alloy, it exhibits twice the yield strength, an increase in uniform elongation from 16.2 % to 24.2 %, and a higher ultimate tensile strength (UTS) of 1.5 GPa.

Despite the aforementioned successes, numerous fundamental questions regarding HS-HEAs remain unanswered. For example, are heterostructures in HEAs equivalent to those in traditional alloys when the same processes are employed? Does the optimal volume fraction of hard and soft zones directly apply to HEAs as well? It's worth noting that in HSMs prepared by partial recrystallization processes, the recrystallized regions typically represent the soft zone, while regions with high dislocation densities, such as ultrafine-grained and unrecrystallized regions, constitute the hard zone [16,17,20]. However, HEAs continue to exhibit exceptional properties even when they are fully or nearly fully recrystallized, i.e., deviate significantly from the ideal heterostructure [22–25]. For instance, both 40 % and 80 % recrystallized CoCrNi alloys demonstrate impressive combinations of properties [24]. This observation raises the possibility that heterostructures in HEAs may differ from their conventional counterparts.

In this study, CoCrFeNi is selected as a model system to study heterostructures in HEAs. Unlike alloys used in previous HS-HEA studies, which are mostly multi-phased, CoCrFeNi is a single-phase FCC alloy [6, 33–35]. It is often used as a base alloy to which additional elements are added to create a diverse range of pseudo-binary or pseudo-ternary alloys for theoretical study or various applications [36–45]. Moreover, in contrast to CoCrNi and CoCrFeMnNi, which are characterized by their low stacking fault energy and therefore prevalent deformation twinning, CoCrFeNi possess a higher stacking fault energy [10,46-48]. This leads to a simple dislocation-mediated deformation that barely involves deformation twinning, which allows us to focus more on heterostructure itself. By employing simple cold rolling and annealing procedures, we produced three HS-HEAs with varying degree of recrystallization. Our analysis shows that the hard and soft zones in HEAs are different from general expectation. Contrast to conventional hard zone with high dislocation density, the existence of dislocation-free recrystallized hard zone (RHZ) is discovered. The existence of RHZ leads to a unique tri-modal heterostructure that enables excellent mechanical performances.

2. Experimental procedures

The CoCrFeNi alloys were prepared by vacuum arc melting under a high purity argon atmosphere. Raw materials (purity $\geq$ 99.95 %) were placed in a water -cooled copper mold and melted for four times to enhance chemical homogeneity. The ingots ($50 \times 25 \times 8$ mm³) were homogenized in vacuum at 1100 °C for 24 h and then cold-rolled to sheets with thickness of 1 mm (87.5 % reduction). The sheets were subsequently annealed in air at 600, 650, and 700 °C for 5 min to obtain three different HSMs (henceforth called HSM1, HSM2, and HSM3,

respectively).

Microstructure observations were carried out using a JOEL-5400 scanning electron microscope (SEM). Crystal structures were analyzed by a BRUKER-D8 Discover X-ray diffractometer operated at 40 kV and 30 mA using Cu Kα radiation. Electron backscatter diffraction (EBSD) technique was performed using an Oxford NordlysMax 3 EBSD instrument on a JOEL JSM-7800F SEM. Mechanical polishing was applied to the specimens before metallographic observation. Transmission electron microscopy (TEM) observations were carried out using a JOEL JEM-2100F microscope and high-resolution transmission electron microscopy (HRTEM) images were taken on a JEOL JEM-ARM300F2 equipped with double spherical aberration correctors. TEM samples were prepared by initially grinding and polishing them to a thickness of less than 100 μm, and subsequently twin-jet polished, using an electrolyte comprised of 5 % perchloric acid and 95 % alcohol at a temperature of −25 °C with a voltage of 30 V.

Tensile test samples were cut to gauge dimensions of 16 mm x 6 mm x 1 mm and tested with a Shimadzu AGS-1000 kN universal tensile machine with a strain rate of 1×10^{-3} s^{-1}. Repetitive loading-unloading-reloading tests were conducted for HSM2 and HSM3. The loading/reloading strain rate was 5×10^{-4} s^{-1}, and a load-controlled unloading rate of 3.3 N/s was applied to reach a minimum load of 200 N. Local hardness of different regions were measured by nano-indentation using a Bruker's Hysitron TI 980 TriboIndenter with a Berkovich diamond indenter tip. The maximum load is 12 mN and the loading rate is 1 mN s^{-1}. To identify the type of region each indent represents (which will be explained later), EBSD scans were performed before and after indentation. Data from indents located in mixed regions whose type cannot be clearly distinguished is discarded. At least 50 indentation data is collected for each type of region.

3. Results

3.1. As-homogenized and as-rolled microstructure

Fig. 1a shows the microstructure of the as-homogenized (as-homo) CoCrFeNi alloy, equiaxed grains with an average grain size of 850 μm are observed. After 87.5 % cold rolling, dense shear bands resulting from plastic deformation form a complex, network-like structure (Fig. 1b). TEM analysis shows the presence of high-density dislocations and
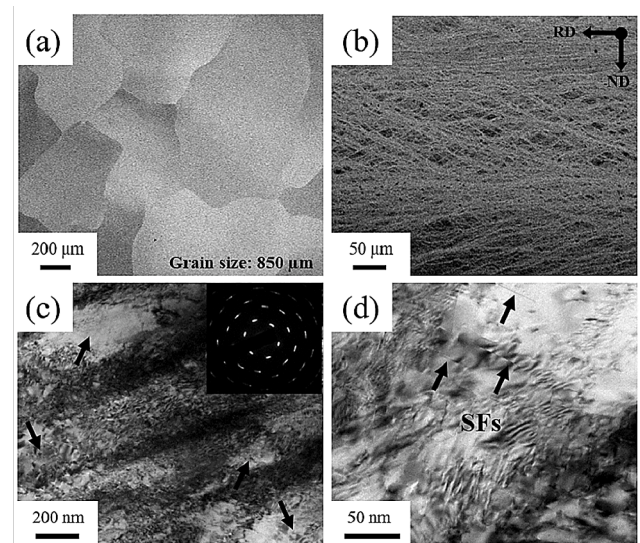

Fig. 1. SEM images of (a) the as-homo and (b) the as-rolled CoCrFeNi alloy; (c) (d) show the TEM bright field images of the as-rolled alloy. Inset shows the corresponding SADP. Arrows in (c) indicate dislocation cells and those in (d) indicate stacking faults.

dislocation cells (Fig. 1c). From the selected area diffraction pattern (SADP), it can be observed that the diffraction spots have extended into short arcs, indicating slight angular variations. Besides typical dislocation substructures, only a small amount of stacking fault can be observed (Fig. 1d). Thus, the plastic deformation is dominated by dislocation activities, which is consistent with previous literature [34,35].

3.2. A first look at the microstructure

According to X-Ray diffraction, all three HSMs remain a single-phase FCC structure after annealing (Fig. S1). However, annealing at different temperatures results in varying degrees of recrystallization (Fig. 2). HSM1 is annealed at the lowest temperature, and the majority of the alloy remain unrecrystallized (Figs. 2a-c). Fig. 2b shows the distribution of the recrystallized grains by blackening out the unrecrystallized regions. The recrystallized regions are approximately 27 % in volume fraction, and they form lamellas that are tens of micrometers long (Fig. 2b). These constitute the "ideal" heterostructure predicted to provide the best properties: lamella-shaped soft zones with approximately 20–30 % volume fraction embedded in a hard zone matrix [17, 20]. The microstructure of HSM2 is somewhat inverse to that of HSM1 (Figs. 2d-f), with unrecrystallized hard zones (UHZs, vol. fraction 37.9 %) embedded in the recrystallized soft zones (RSZs, vol. fraction 62.1 %). Such structure is far away from the ideal heterostructure, and is anticipated to exhibit inferior properties. HSM3 is annealed at the highest temperature, and therefore have almost completely recrystallized (Figs. 2g-i). Its structure is composed of large-grained regions surrounded by a fine-grained matrix. The recrystallized grains in all three HSMs were relatively small, with their sizes measuring approximately 1 μm, 1.8 μm, and 1.9 μm, for HSM1, 2, and 3 respectively. This suggests that a large proportion of grains are smaller than 2 μm.

3.3. Mechanical behaviors of the HSMs

The tensile curves of the HSMs are shown in Fig. 3a, and important numbers from the curves can be found in Table 1. The as-rolled alloy exhibits high strength but very low uniform elongation (UEL, 1.7 %). In contrast, the as-homo alloy demonstrates high elongation but a YS of only 146 MPa, showing a typical strength-ductility trade-off. Surprisingly, despite having an ideal heterostructure, HSM1 exhibits mechanical properties similar to the as-rolled alloy. In contrast, HSM2, which features ~38 % of UHZs embedded in a recrystallized matrix, exhibits an excellent strength-ductility combination, having a YS of 817 MPa, an UTS of 953 MPa, and an elongation of 33 %. Interestingly, HSM3, which has almost completely recrystallized, is still four times stronger (in YS) than the as-homo alloy, while remaining a similar elongation.

The work hardening behaviors of the HSMs are shown in Fig. 3b. The hardening rates of both the as-rolled alloy and HSM1 drop in a free-fall manner, while that of the as-homo alloy shows a gradual monotonic decrease typical of coarse-grained materials. The hardening rate of HSM3 shows an inversion after the initial drop, and then remains at a level similar to that of the as-homo alloy until ~27 % true strain. Such discontinuous yielding is typical for heterogeneous materials, indicating that hetero-effect is indeed working in HSM3. HSM2 exhibits an unusual secondary discontinuous yielding behavior following the standard initial discontinuous yielding, this will be discussed later.

The outstanding mechanical properties demonstrate the efficacy of the heterogeneous design in the CoCrFeNi alloy. Fig. 3c compares the YS and UEL of CoCrFeNi in various processing states, including different homogeneous states via conventional processes and ultrafine-grained states via high pressure torsion. It can be seen that CoCrFeNi with a homogeneous structure faces the common strength-ductility trade-off, while our heterogeneous approach using simple cold rolling and
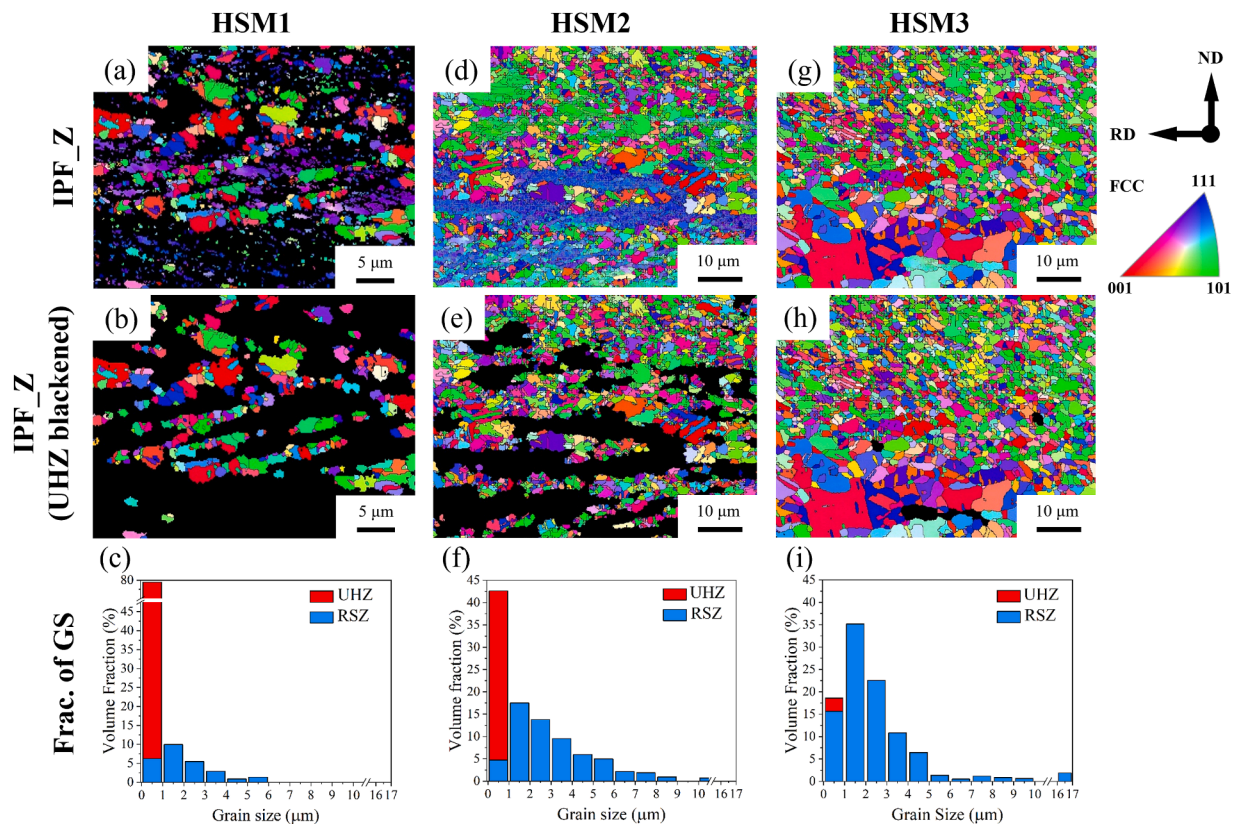

Fig. 2. Inverse pole figure (IPF_Z) maps and grain size distributions of (a-c) HSM1, (d-f) HSM2, and (g-i) HSM3. The top row shows IPF_Z maps, where black signifies unidentified uncrystallized regions due to deformation. The middle row shows the corresponding IPF_Z maps after blackening out all the unrecrystallized regions for easy recognition. The bottom row shows the volumetric distribution of grain size.
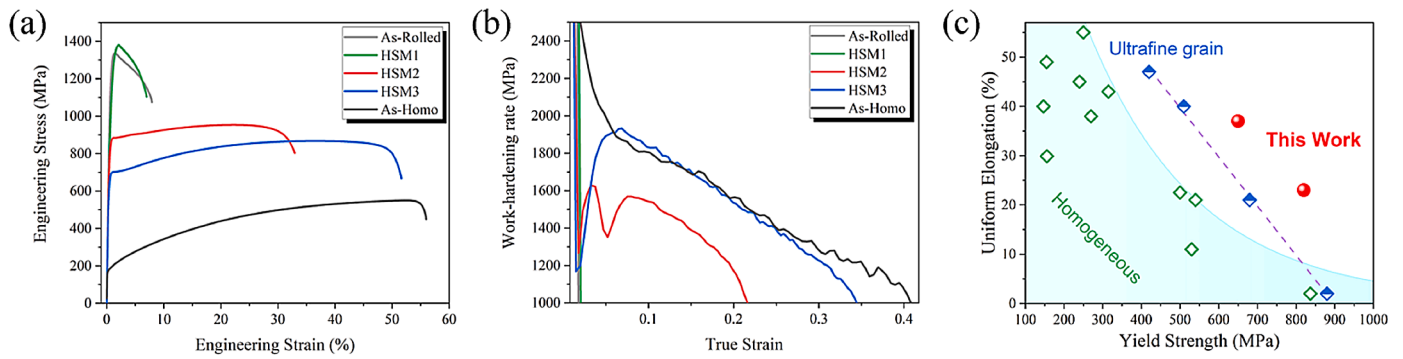
Fig. 3. (a) Engineering stress-strain curves and (b) work hardening curves of CoCrFeNi processed under different conditions. (c) Yield strength vs. uniform elongation of CoCrFeNi in various states collected from literature [6,49-56] and those for our HSMs.

Table 1
Tensile properties of CoCrFeNi under different processing conditions in this work.

	YS (MPa)	UTS (MPa)	UEL (%)	EL (%)
As-rolled	1159	1361	1.7	4.8
HSM1	1120	1302	1.9	6.4
HSM2	817	953	22.1	32.9
HSM3	650	868	36.8	51.7
As-homo	146	550	52.3	56.0

annealing overcomes this problem. Our HSMs even outperform ultrafine-grained CoCrFeNi obtained through high pressure torsion. Representing the best mechanical property combination there is for CoCrFeNi.

Fig. 4a shows the true stress-true strain curves of HSM2, HSM3, and the as-homo alloy obtained by loading-unloading-reloading tests. All unloading-reloading cycles exhibit detectable reverse plastic flow hysteresis, indicating the presence of non-uniform deformation in all samples. Interestingly, during each loading-unloading-reloading cycle, HSM2 and HSM3 display more pronounced hysteresis loops than the as-homo alloy (Fig. 4b), indicating that hetero-structures exhibit higher hetero-deformation induced strengthening effect than homogeneous structures. According to the literature [57], the hetero-deformation induced strengthening stress (σ_{HDI}) can be calculated by the equation:

$$\sigma_{HDI} = \frac{\sigma_r + \sigma_u}{2}$$

where the reloading yield stress σ_r and unloading yield stress σ_u can be measured from each hysteresis loop in Fig. 4b. The variation of σ_{HDI} as a function of strain is provided in Fig. 4c. At the same strain level, HSM2 exhibits higher hetero-deformation induced stress, aligning with the

results reflected in the hysteresis curve in Fig. 4b and confirming the reliability of σ_{HDI} measurements. The initial σ_{HDI} of HSM2 is 456 MPa, while that of HSM3 is 386 MPa. Both of them clearly surpass the as-homo alloy (117 MPa). After reaching uniform elongation, the maximum σ_{HDI} for HSM2 and HSM3 is 612 and 544 MPa, respectively. Notably, the maximum σ_{HDI} for the as-homo alloy increases to 484 MPa. Due to the presence of texture and grain boundaries, even in a homogeneous structure, microscopic plastic inhomogeneity can occur [58–60]. Deformation in the vicinity of grain boundaries triggers the activation of geometrically necessary dislocations across multiple slip systems, resulting in orientation gradients characterized by lattice rotations [61,62]. Consequently, under high strain, the accumulation of geometrically necessary dislocations near grain boundaries in the as-homo alloy generates hetero-deformation induced stress, resulting in stress-strain hysteresis during unloading and reloading.

3.4. Further analysis of the microstructure

As shown previously, despite the seemingly ideal heterostructure in HSM1, its mechanical properties are similar to the as-rolled alloy. In contrast, HSM2, which features UHZs embedded in a recrystallized matrix, exhibits an excellent strength-ductility combination. Further analysis is therefore conducted in HSM2 to investigate microstructural features that could lead to such scenario. The microstructure of the recrystallized regions in HSM2 comprises isolated large grains (called large-grained region, LGR) surrounded by a small-grained matrix (called small-grained region, SGR) (Fig. 2d-i) which is somewhat similar to that of HSM3. Figs. 5a-b present a high-magnification EBSD analysis of a small-grained region (with grain sizes ≤ 2 µm). Several features are noted. Firstly, the average grain size in the fine-grained region is remarkably small, approximately 0.46 µm according to our EBSD analysis. This is in stark contrast to just-recrystallized microstructures (i.e.
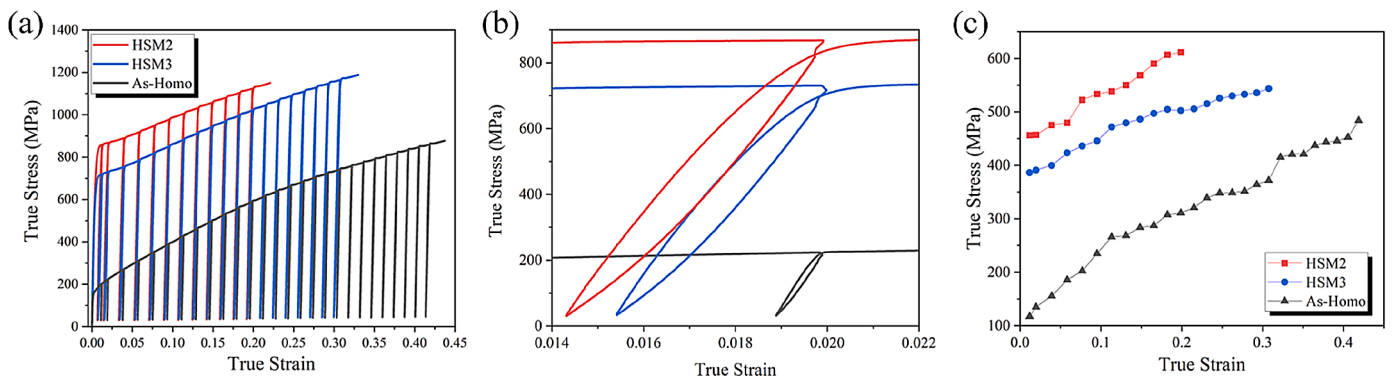

Fig. 4. (a) True stress-true strain curves of CoCrFeNi processed under different conditions using loading-unloading tensile tests; (b) magnified unloading-reloading hysteresis loops taken from (a); (c) hetero-deformation induced stress derived from the unloading-reloading hysteresis loops.
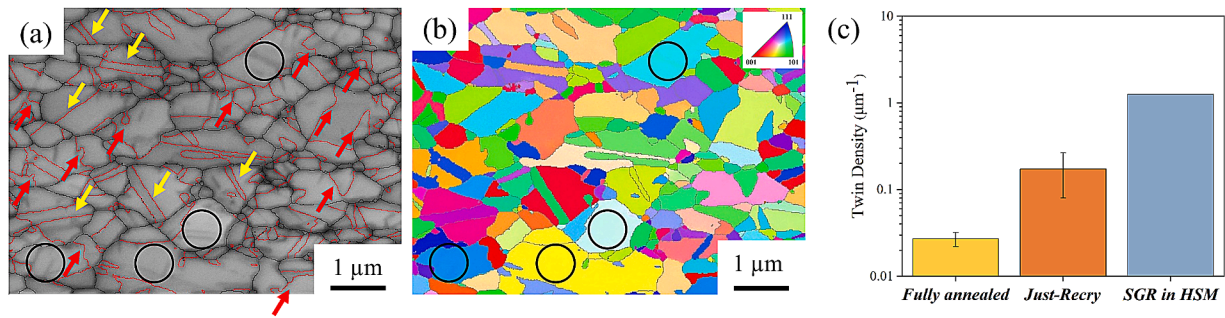
Fig. 5. (a) Band contrast image and (b) IPF_Z of the SGR in HSM2; (c) Twin densities in the SGR of HSM2 compared to those in various fully-annealed and just-recrystallized conventional alloys. Yellow and red arrows in (a) indicate coherent twin boundaries and incoherent twin boundaries, respectively.

grain growth has barely begun) in conventional alloys, where grain sizes typically range from tens to hundreds of micrometers (see Table S1). Even in heavily alloyed conventional metals, just-recrystallized grain sizes are still in the range of 5–10 μm. Secondly, the twin density in the SGR is exceptionally high, measuring 1.26 μm^{-1} (using the approach in Ref. [63]). This value is two orders of magnitude higher than those in fully annealed conventional alloys and still one order of magnitude higher than those in just-recrystallized ones (Fig. 5c and Table S2). In fact, we suspect that the actual twin density is higher because many twin boundaries seem to be omitted in Fig. 5a-b (black circles) due to insufficient resolution of the EBSD technique. Thirdly, unlike most annealing twins, which generally have coherent twin boundaries (yellow arrows in Fig. 5a), a significant faction of twin has incoherent twin boundaries (red arrows). This is evidenced by the abundant non-linear twin boundaries in Fig. 5a.

Further TEM observations of the recrystallized grains in HSM2 (Fig. 6a) show that the actual twin density is apparently higher than what EBSD can resolve. Surprisingly, we noticed a strong dependence of twin density on grain size. Small grains exhibit extremely high twin densities and nanoscale twin widths (~20 nm, see Fig. 6a). In contrast, large grains show lower twin densities with wider twin widths (~1 μm, Fig. 6b). Through examining numerous grains, it is concluded that the critical grain size for this stark contrast is around 2 μm. As twin boundaries are strong obstacles for dislocations [64], the prevalence of twins reduces the effective size of these grains. We analyzed the effective grain sizes using the intercept method (Fig. 6c). The effective grain size decreases linearly with grain size initially, then abruptly stabilizes at a constant value of 129 nm for grain sizes below 2 μm. This indicates an enhanced refinement effect in grains below the critical size. The clear difference in twin densities between small grains and large grains suggests that their properties could also be significantly different, as will be

evidenced later. Thus, the recrystallized regions should indeed be further divided into SGR and LGR, with the strength of the former expected to be noticeably higher. This leads to a tri-modal microstructure with three structural components: SGR, LGR and UHZ.

3.5. Deformation behavior

To assess the distinct deformation behaviors of the two recrystallized regions (SGR and LGR) in HSM2, we conducted kernel average misorientation (KAM) analysis at 0 %, 5 %, and 10 % tensile strain, as shown in Fig. 7 and Table 2. The IPF_Z image and the KAM map revealed that UHZs already exhibited high misorientation at 0 % strain, indicating a high defect density resulting from cold work (Figs. 7a-7b). Recrystallized grains have clearly lower misorientation at 0 % strain. However, SGR exhibited higher misorientation compared to LGR, possibly due to the presence of high-density twin boundaries not resolved by EBSD. At 5 % strain, the deformation of LGR has clearly taken place. The KAM map turned greener, with a recorded KAM increment of 0.13. In contrast, there was no significant KAM increment for both UHZ and SGR, with KAM increments of 0 and 0.01, respectively. This suggests notable strain partitioning, with the LGR primarily accommodating the deformation. After reaching 10 % strain, KAM in LGR further increased, while KAM in UHZ remained unchanged. The KAM in SGR, however, started to increase significantly. This implies a second stage of strain partitioning occurring between 5 % and 10 % strain, with SGR starting to participate in the deformation. Therefore, in the tri-modal microstructure of HSM2, the initiation of deformation in SGR is indeed delayed to a higher strain level, resulting in a more complicated strain partitioning scenario.

Fig. 8 shows the deformation microstructure of HSM2 after 2 % and 10 % strain. At 2 % strain, planar dislocations are observed in the LGRs. The dislocations often accumulate at the zone boundaries, forming
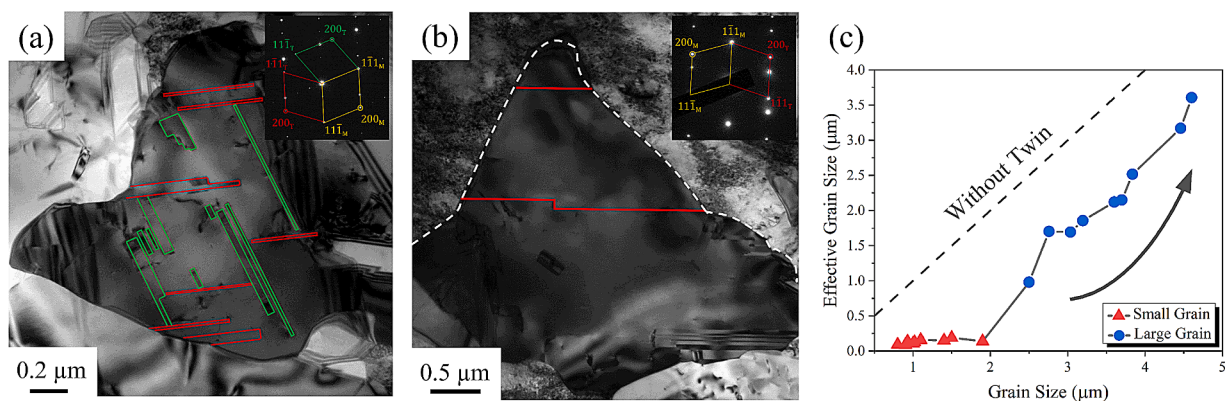

Fig. 6. Representative TEM images of (a) small grains and (b) large grains in HSM2. Inset shows the SADP of the center grain. (c) Grain size versus effective grain size for grains in HSM2. The solid lines in (a-b) represent twin boundaries, with colors corresponding to the twin spots in the SADP. The white dashed lines denote zone boundaries.
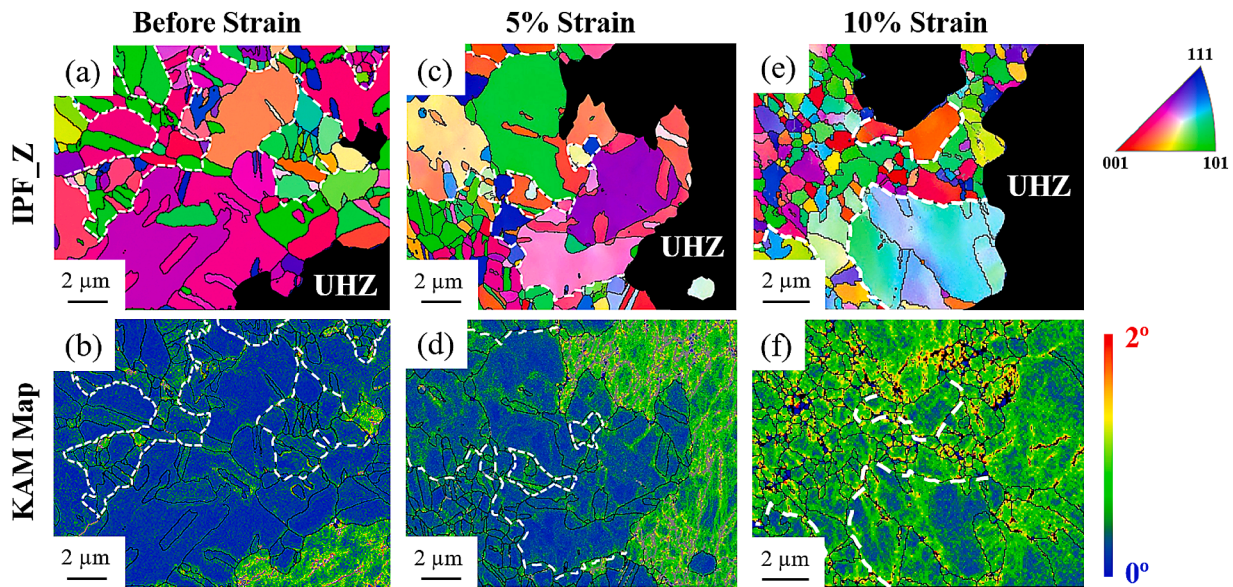
Fig. 7. (a, c, e) IPF_Z maps and (b, d, f) KAM maps of HSM2 before strain, after 5 % strain, and after 10 % strain. UHZs are blackened in the IPF_Z maps and white dotted lines indicate boundaries between SGR and LGR.

Table 2
KAM in UHZ, SGR, and LGR of HSM2 after different degrees of strain.

Region	Misorientation (°)				
	0 %	5 %	10 %	Increment after 5 %	Increment after 10 %
UHZ	0.96	0.96	0.96	0.00	0.00
SGR	0.34	0.35	0.72	0.01	0.37
LGR	0.22	0.34	0.73	0.12	0.51

dislocation pile-ups (Fig. 8a). Zhu et al. suggest that this type of geometrically necessary dislocations assembly is the most effective in producing back stress [18]. In contrast, the density of dislocations in the grains of SGR are evidently lower. This agrees well with our KAM results. At 10 % strain, dislocation densities increase evidently in both SGR and LGR. However, dislocations clearly tend to accumulate at both grain boundaries and twin boundaries (Fig. 8c). This is further evidenced by HRTEM analysis. Regions away from twin/grain boundaries exhibit few dislocations (Fig. 8d). In contrast, regions adjacent to twin boundaries display a very high dislocation density (Fig. 8e). Hence, it can be concluded that at this strain (10 %), the SGRs already participate in deformation, and the twin boundaries indeed effectively hinder dislocation movement and produce dislocation pile-ups.

4. Discussions

4.1. The origin of dense nanoscale twins and their strengthening effects

The microstructure within the small-grained region (SGR) belongs to a just-recrystallized structure that has not undergone grain growth. This structure differs significantly from fully annealed microstructures. The latter typically exhibit grain sizes in the range of hundreds of micrometers, very low twin density, large twin widths, and coherent twin boundaries. In contrast, microstructures immediately after recrystallization display smaller grain sizes, narrower twin widths, and abundant incoherent twin boundaries [65]. In fact, due to the distinct twin morphologies arising from these two states, it has been proposed to designate them with more specific terms – recrystallization twins and grain growth twins, instead of collectively referring to both as annealing twins [66].

In the early stage of recrystallization, the newly formed grains

exhibit significant misorientation with respect to the deformed matrix. When the grain boundaries of these new grains migrate into the deformed matrix, they undergo high-angle plane rotations that evidently impede the rate of grain growth [67]. To accelerate grain boundary migration, these new grains transform their orientation by producing twins to overcome the misorientation with the deformed matrix [68–71]. The 1st generation of twins continue this process and produce multiple generations of twins. This is called the multiple twinning mechanism, and is known to result in exceptionally high twin density [65,66,70-72]. Multiple twining plays a critical role in filling the orientation space and transforming the texture of the deformed matrix into a fully recrystallized texture. In this process, when grains with twin orientation come into contact with grains of different generations of twins, incoherent twin boundaries are produced [73]. This explains the abundance of incoherent twin boundary in just-recrystallized microstructure. Since the boundary energy of coherent twins is only 1/10 that of incoherent twins [74], when grain growth begins, most incoherent twin boundaries will soon disappear [66]. Consequently, the remaining twins after grain growth are mostly coherent.

Although the SGRs in our heterostructured materials (HSMs) clearly exhibit features of just-recrystallized microstructures, they also exhibit features distinct from just-recrystallized microstructures in conventional alloys. Firstly, the sizes of just-recrystallized grains in conventional alloys are typically tens to hundreds of micrometers, and are still at least 5–10 μm even for heavily alloyed, low stacking fault energy alloys (Table S1). In contrast, the average sizes of all recrystallized grains in our three HSMs are all less than 2 μm. Secondly, the twin widths in just-recrystallized conventional alloys are micrometer-sized, whereas those in the SGRs of our HSMs are only around 20 nm. Thirdly, the twin density in the SGRs is an order of magnitude higher than those in just-recrystallized conventional alloys (Fig. 5c). These differences can be attributed to two factors in the recrystallization behavior of HEAs, which set them apart from conventional alloys.

The first is the evidently lower grain growth rate in HEAs. In conventional alloys, grain boundaries tend to move at an excessively fast rate during recrystallization, resulting in recrystallized grains tens or hundreds of microns in size by the time recrystallization is completed. In HEAs, however, it is known that diffusion is more sluggish due to a greater fluctuation in lattice potential energies [75]. This constraint slows down the migration of grain boundaries. In fact, boundary migrations are further hindered by the significant solute drag effect in
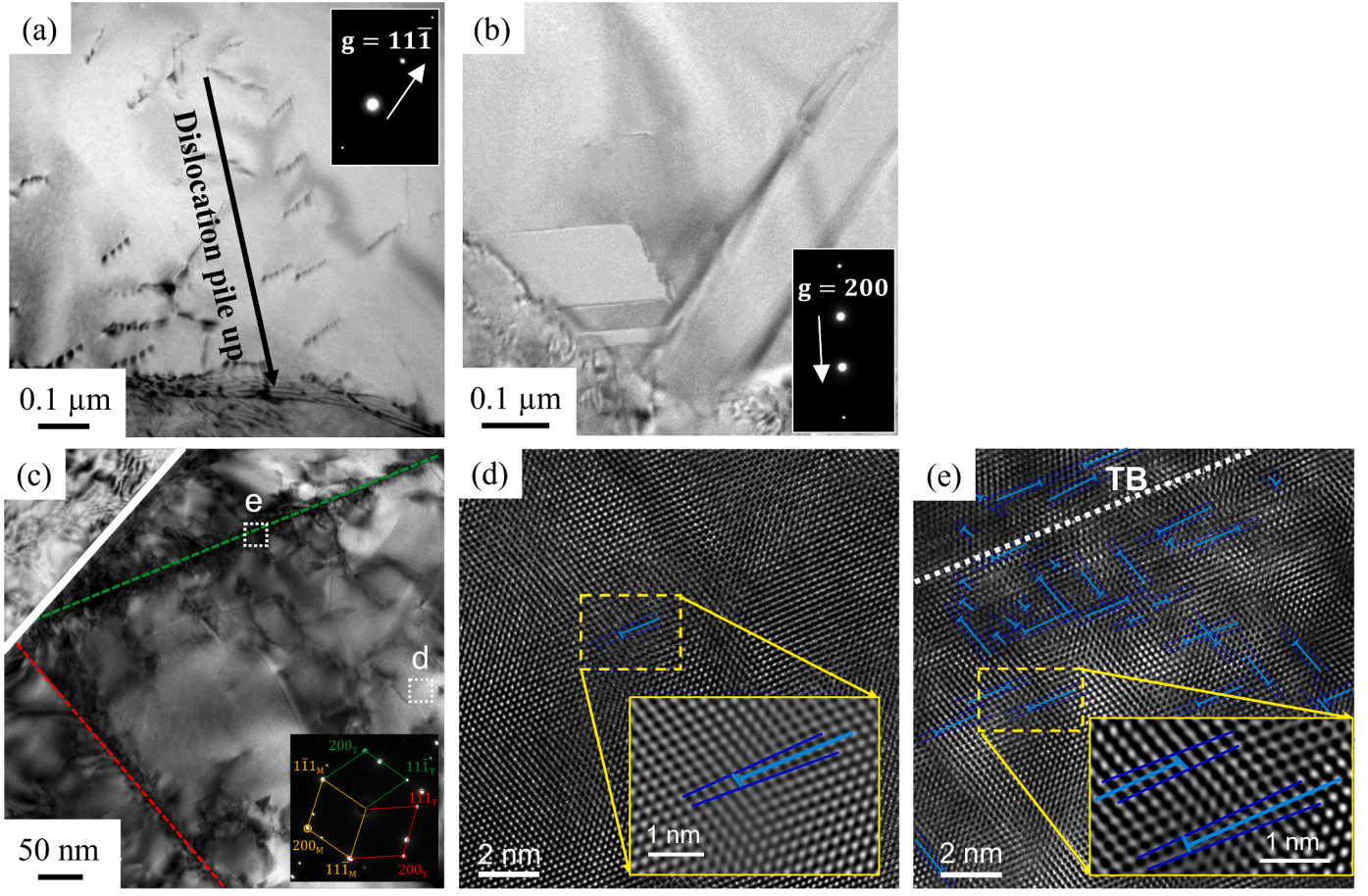
Fig. 8. Representative TEM images of HSM2 after deformation. (a) Large grains and (b) small grains after 2 % strain; (c-e) Microstructure within small grains after 10 % strain. (c) Bright-field image with corresponding SADP, twins are marked by green and red dash lines. (d) HRTEM image in regions away from grain/twin boundaries (region d in (c)). (e) HRTEM image adjacent to twin boundaries (region e in (c)). Insets in (d) and (e) show magnified inverse fast Fourier transform images of the yellow rectangles.

HEAs, which originates from their complex composition where all the components can be regarded as solutes [76,77]. These mechanisms reduce the boundary migration rate and raises the activation energy for grain growth. For instance, the CoCrFeMnNi alloy exhibits an activation energy for grain growth (321.7 kJ/mol^{-1}) twice that of AISI 304LN [78]. The low grain growth rate thus enables the extremely fine grain size at the end of recrystallization, which is crucial for retaining the high twin density and the formation of recrystallized hard zones. The second factor is the lower energy penalty for twin formation in HEAs. This is because the "perfect" lattice in HEAs is inherently distorted due to the atomic size differences between different elements (i.e. severe lattice distortion effect [1,2]). Therefore, the activation energy for twin nucleation and the energy difference between a "perfect" lattice and one with twin boundary are both reduced [1,79,80]. Consequently, HEAs have a higher propensity to form twins and a lower driving force to eliminate twin boundary – both critical to achieve the high twin density observed in the SGR of our HS-HEAs.

Such high twin density is expected to evidently strengthen the SGRs. The strengthening effect can be estimated quantitatively using the Hall-Petch equation [81,82]:

$$\sigma_y = \sigma_0 + \frac{k_{HP}}{\sqrt{d}} \quad (1)$$

where σ_y is the predicted YS, σ_0 is the lattice friction stress, k_{HP} is the Hall-Petch slope [83], and d is the average grain size. Eq. (1) can be modified for the SGRs and the large-grained regions (LGRs) as follows to account for their respective effect of twins:

$$\sigma_{SGR}^* = \sigma_0 + \frac{k_{HP}}{\sqrt{d_{SGR}^*}} \quad (2)$$

$$\sigma_{LGR}^* = \sigma_0 + \frac{k_{HP}}{\sqrt{d_{LGR}^*}} \quad (3)$$

where σ_{SGR}^* and σ_{LGR}^* represent the predicted YS for SGR and LGRs after considering the strengthening effect of twins, respectively. d_{SGR}^* and d_{LGR}^* represent the effective grain sizes for SGRs and LGRs measured by TEM. Table 3 lists the parameter values used in our calculation and the predicted results. The predicted YS of the SGR is 891 MPa, while that of the LGR is only 328 MPa. Therefore, the former is 2.7 times stronger than the latter. Considering that the YS of the as-rolled alloy being 1159 MPa (Table 1), it is evident that the strength of SGR is comparable to that of the unrecrystallized hard zone (UHZ). These calculations are further evidenced by nano-indentation experiments, by which the hardness values of UHZ, SGR and LGR are measured (Fig. S2). The hardness values of UHZ and SGR are 4.2 and 4.0 GPa, respectively, while that of LGR (3.1 GPa) is noticeably lower. It is worth noting that the difference in hardness between SGR and LGR will not be as significant as that in YS

Table 3
Predicted YS for SGR and LGR in HSM2 and the parameter values used for the prediction. Values of σ_0 and K_{HP} for CoCrFeNi are taken from Ref [83].

σ_0 (MPa)	K_{HP} (µm$^{-1/2}$)	d_{SGR}^* / d_{LGR}^* (µm)	σ_{SGR}^* / σ_{LGR}^* (MPa)
123	276	0.129 / 1.182	891 / 328

between the two. This is because hardness reflects UTS much better than YS in highly deformable FCC HEAs due to the contribution of their strong work hardening to hardness [84]. As a reference, we also measured the hardness of the As-Homo alloy. Its nano-indentation hardness is 2.6 GPa. Clearly, the behavior of LGR is similar to that of the As-Homo material, while the behavior of SGR is similar to that of the As-Rolled material. These results align well with our calculations. Hence, unlike heterostructured conventional alloys, where regions recrystallized from cold work are always regarded as soft zones, the exceptionally high twin density in the SGR seems to turn them into unique **recrystallized hard zones** (RHZs).

It should be noted that LGR and SGR share a common formation mechanism, but were formed at different annealing stages. This is because the defect densities induced by the cold rolling process is non-uniform, leading to distinct rates of recrystallization nucleation in the deformed matrix. As annealing progresses, recrystallization and grain growth occur simultaneously, resulting in the coexistence of regions with larger and smaller grains. Therefore, as grain growth proceeds, SGRs will gradually turn into LGRs.

4.2. Reconsidering the hetero-zones in HEAs

In HSMs, the hard zones typically consist of regions with high dislocation density, such as unrecrystallized or ultrafine-grained regions, while the soft zones include all regions with low dislocation density. Zhu et al. suggested that embedding 25–30 vol.% of soft zone in a hard matrix will result in optimal mechanical properties through hetero-deformation induced related effects. However, in this study, the behavior of HS-HEA appears to be different. Table 4 shows the volume fractions of UHZ, SGR, and LGR in each HSM. Based on previous definition, unrecrystallized region should be the hard zone and recrystallized regions should serve as the soft zone. Therefore, HSM1 should have been the optimal HSM, given its composition of 73 % hard zone (UHZ) and 27 % soft zone (SGR + LGR). However, its UEL is only 1.9 %, similar to the as-rolled alloy. Surprisingly, HSM2, which contains only 38 % UHZ, exhibits the best combination of strength and ductility and high hetero-deformation induced stresses. Furthermore, HSM3, nearly fully recrystallized, exhibits over four times the YS of the as-homo alloy, while maintaining similar ductility. This suggests that HSM3 is also a promising HSM.

The discrepancy between expected and actual properties can be understood by the formation of the RHZ (i.e., the SGR), this is illustrated in Fig. 9. Owing to the formation of dense nanoscale twins in the SGR, its effective grain size is reduced to only 129 nm. As demonstrated in Section 4.1, this results in significant strengthening, making the YS of the SGR about 2.7 times that of the LGR. Given that the YS of the UHZ is about 3.5 times that of the LGR, it is clear that the SGR resembles the UHZ far more than the LGR. Our KAM mapping results also show evident strain partitioning between LGR and SGR at low strain. These results suggest that the SGR should be regarded as a hard zone instead of a soft zone as in the case of conventional metals. If we now acknowledge SGR as a hard zone, the volume fraction of hard zone in HSM1 becomes 90 % (Fig. 9b), which explains its poor ductility. The fraction of hard zone in HSM2 increases to 60 %, which is closest to the ideal fraction, making it the best among the three HSMs. HSM3 has a largest increase in hard zone fraction (from 3 % to 54 %). This value is farther away from the ideal value, yet is still sufficient to exhibit some heterogeneous effect,

which aligns with the high strength and high hetero-deformation induced stress observed. Based the above, acknowledging the existence of RHZ is of critical importance in understanding the properties and designing the microstructures of HS-HEAs.

4.3. The tri-modal microstructure and its benefits

Table 4 displays the volume fractions of UHZ, SGR, and LGR in our HSMs. HSM1 is primarily composed of UHZ, whereas HSM3 consists of nearly equal amounts of SGR and LGR. In contrast, HSM2 contains a comparable fraction of the three zones, resulting in a unique tri-modal microstructure that is rarely reported in HSMs. Such a tri-modal structure exhibits unique deformation behavior. At low strain levels, deformation is concentrated in the soft zone as in common bi-modal HSMs. Indeed, KAM analysis (Fig. 7d) indicates that near 5 % strain, the two hard zones have hardly deformed. However, at 10 % strain, RHZ has started to deform significantly, while UHZ's deformation remains very limited (Fig. 7 and Table 2). This implies that the tri-modal structure introduces two-stage strain partitioning. This phenomenon can also be observed in HSM2's hardening curve. In the early stage of deformation (before 3.5 %), a discontinuous yielding typical of HSMs appears. Discontinuous yielding is usually attributed to the lack of mobile dislocations in the soft zone at the beginning of its deformation. As RHZ is still hardly deformed at 5 % strain, this should correspond to the onset of deformation in LGR. However, an unusual second discontinuous yielding event occurred after the first (at 3.5–8 %). Since the RHZ is the only zone that start to deform evidently after 5 % strain, the second discontinuous yielding should originate from onset of deformation in the RHZ. Thus, the two-stage strain partitioning is further evidenced by the two discontinuous yielding events. The tri-modal microstructure and its distinct deformation behavior offers several advantages:

Superior balance between strength and ductility contributed by RHZ. The primary distinction between the two hard zones lies in their strengthening mechanism. UHZ derives its strength from forest dislocation strengthening, a result of their nearly saturated dislocation density. Conversely, RHZ attains its strength from an exceptionally high interface density, following the Hall-Petch strengthening mechanism. This distinction results in the former barely having hardening capability, while the latter exhibits excellent hardening ability. The hardening ability of RHZ is demonstrated in HSM3, which comprises as much as 51 % of RHZ. Its hardening ability remains almost identical to that of the as-homo alloy over a wide range of strain (Fig. 3b). This enables HSM3 to achieve an YS increase of ~4.5 times compared to the as-homo alloy, while experiencing only a minimal loss in ductility (EL still 52 %). Consequently, when compared to the traditional UHZ, RHZ provides a superior balance between strength and ductility.

More zone boundaries and stronger hetero-deformation induced effects. In HSMs, boundaries between soft and hard zones play a key role since strain partitioning and associated hetero-deformation induced strain hardening take place around them. However, within our tri-modal microstructure, the notable difference in deformability between RHZ and UHZ lead to strain partitioning between these two hard zones at elevated strains. As a result, even the boundaries between the hard zones can contribute to hetero-deformation induced strain hardening. According to EBSD analysis, the densities for the three types of zone boundaries in HSM2, namely UHZ/LGR, RHZ/LGR, and UHZ/RHZ, are 0.109, 0.343, and 0.221 μm^{-1}, respectively, totaling 0.673 μm^{-1}. In comparison, those for HSM3 are 0.008, 0.431, and 0.006 μm^{-1}, respectively, totaling 0.445 μm^{-1}. Thus, HSM2 and HSM3 have similar densities of soft/hard zone boundaries (UHZ/LGR + RHZ/LGR). However, since the former contains additional hard/hard zone boundaries, its overall zone boundary density is 34 % higher than the latter. These additional boundaries are expected to contribute extra hetero-deformation induced hardening effect. Indeed, since HSM2 contains 38 % of UHZ (Table 4), which essentially lacks hardening capability, its overall work-hardening ability is expected to be significantly lower than
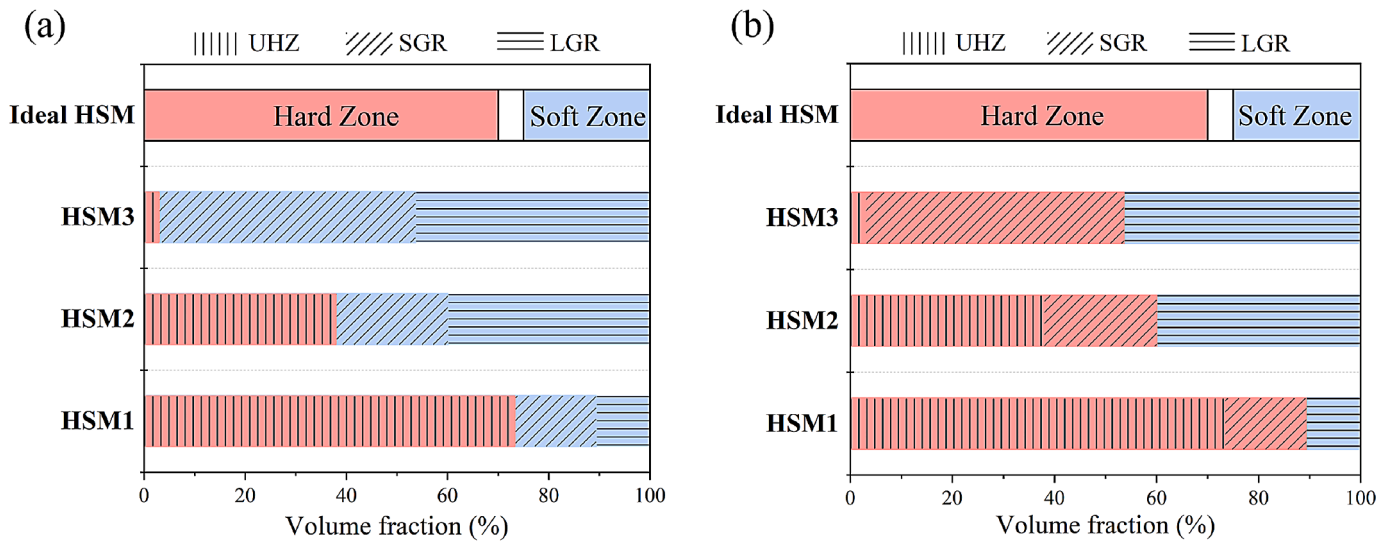
Table 4
Volume fractions of UHZ, SGR and LGR in each HSM.

Region	Volume fraction (%)		
	HSM1	HSM2	HSM3
UHZ	73.3	37.9	2.9
SGR	16.2	22.2	50.8
LGR	10.6	39.9	46.3

Fig. 9. Volume fractions of soft and hard zones in our HSMs when (a) not considering and (b) considering SGR as RHZ. Hard and soft zones are colored red and blue, respectively. Ideal volume fractions of hard/soft zones are also shown at the top, where the white area can be either hard or soft zone.

HSM3 (given similar soft/hard zone boundary densities and recrystallized grain sizes). However, Fig. 3b shows that after the discontinuous yielding events, HSM2′s work-hardening rate is still about 85 % of HSM3′s. This suggests that additional factors enhance HSM2′s work-hardening ability. It is likely that these extra zone boundaries provide HSM2 with increased hetero-deformation induced strain hardening.

Postponed deformation of the RHZ and delayed necking. As mentioned previously, due to the tri-modal microstructure, the deformation of RHZ is delayed until higher strains. This is expected to evidently benefit the alloy's ductility. According to Considère's criterion, necking occurs when the work hardening rate lags behind the true stress. Therefore, to delay necking and enhance ductility, it is essential to maintain a sufficient hardening rate. However, in the early stages of deformation, when stress is low, the required rate of work hardening is not very high. Excessive hardening at this point would unnecessarily consume hardening capacity. In the later stages of deformation, as stress increases, the demand for a higher rate of work hardening also rises. Maintaining a high rate of work hardening at this stage is crucial. Due to the unique nature of the tri-modal structure, the work hardening of RHZ is delayed until higher strains. This implies that a significant part of the hardening capacity (assuming no hardening ability for UHZ and similar hardening ability for RHZ and LGR, that is over 1/3 of the total hardening capability) is kept to the later stages of deformation. Such moderation of strain hardening rate is known to be very effective in delaying necking, as has been demonstrated in medium carbon transformation induced plasticity steels, although the strain hardening rate in that case was moderated by a different strategy [85].

Another factor that may also contribute to the outstanding properties of HSM2 is that its LGR has a near-optimal grain size. Recently, it has been proposed that there exists an optimum grain size for a favorable strength-ductility combination in single-phase metals [86]. This size is approximately two times of l_{Gbar}, which stands for the length of grain boundary affected region. l_{Gbar} is determined by the grain boundary's ability to withstand geometrically necessary dislocation piling-up (or strain gradient accumulation) and can be estimated using the formula:

$$l_{Gbar} \approx \frac{k_{HP}R^{\frac{3}{2}}}{\sqrt{2}MGb} \tag{4}$$

where R is the distance from pinning points to dislocation sources, M is the Taylor factor, G is the shear modulus, and b is the Burgers vector. If substituting k_{HP} with 276 μm^{-1}, R with 0.5 μm, G with 82 GPa, and b with 0.7 μm into the formula, that l_{Gbar} of CoCrFeNi is approximately 0.4

μm [83,86,87]. Therefore, its optimal grain size is around 0.8 μm ($\approx 2l_{Gbar}$). Since the LGR of HSM2 has an effective grain size of about 1.18 μm, which is quite close to this value. This contributes to HSM2 having high strength while maintaining good uniform elongation.

5. Conclusions

The present study produces three HSMs with varying fractions of hard and soft zones by subjecting the CoCrFeNi alloy to simple cold-rolling and partial recrystallization processes. A careful comparison of the structure and properties of these HSMs leads to the following conclusions:

(1) Both HSM2 and HSM3 show good mechanical properties and evident hetero-deformation induced effects. HSM2 shows a YS of 817 MPa and an elongation of 33 %. HSM3 exhibits an elongation similar to the as-homo alloy but its YS is 4.5 times that of the latter.

(2) The formation of dense nanoscale recrystallization twins is observed in small grains with sizes below 2 μm. These twins reduce the effective grain size to merely 129 nm and turn the SGRs into recrystallized hard zones (RHZs). This contradicts conventional understanding, where hard zones are typically regions with high dislocation density rather than clean recrystallized domains.

(3) The emergence of the RHZ imparts an unconventional tri-modal structure to HSM2, encompassing LGR, SGR (i.e. RHZ), and UHZ. Such tri-modal structure results in an enhanced balance between strength and ductility, higher zone boundary density and stronger hetero-deformation induced effects, and a two-stage strain partitioning mechanism that postpones necking. These effects collectively lead to superior overall mechanical properties.

(4) The formation of RHZ significantly alters our understanding regarding the volume fractions, morphologies, and zone boundary density of hard and soft zones. Recognizing the presence of RHZ is therefore pivotal for accurate comprehension of HS-HEAs. Thus, our work provides valuable insights for the future design of HS-HEAs.

CRediT authorship contribution statement

Shu-Yi Tung: Conceptualization, Data curation, Formal analysis,

Investigation, Writing – original draft. **Ting-En Hsu:** Data curation, Investigation. **Yuntian Zhu:** Writing – review & editing. **Ming-Hung Tsai:** Conceptualization, Methodology, Supervision, Writing – review & editing.

Declaration of competing interest

The authors declare that they have no known competing financial interests or personal relationships that could have appeared to influence the work reported in this paper.

Acknowledgements

Supplementary materials

Supplementary material associated with this article can be found, in the online version, at doi:10.1016/j.actamat.2024.119957.

References

[1] M.H. Tsai, J.W. Yeh, High-entropy alloys: a critical review, Mater. Res. Lett. 2 (3) (2014) 107–123.

[2] D.B. Miracle, O.N. Senkov, A critical review of high entropy alloys and related concepts, Acta Mater 122 (2017) 448–511.

[3] Y. Zhang, T.T. Zuo, Z. Tang, M.C. Gao, K.A. Dahmen, P.K. Liaw, Z.P. Lu, Microstructures and properties of high-entropy alloys, Prog. Mater. Sci. 61 (2014) 1–93.

[4] E.P. George, D. Raabe, R.O. Ritchie, High-entropy alloys, Nat. Rev. Mater. 4 (8) (2019) 515–534.

[5] B. Gludovatz, A. Hohenwarter, K.V. Thurston, H. Bei, Z. Wu, E.P. George, R. O. Ritchie, Exceptional damage-tolerance of a medium-entropy alloy CrCoNi at cryogenic temperatures, Nat. Commun. 7 (1) (2016) 10602.

[6] Z. Wu, H. Bei, G.M. Pharr, E.P. George, Temperature dependence of the mechanical properties of equiatomic solid solution alloys with face-centered cubic crystal structures, Acta Mater 81 (2014) 428–441.

[7] Z. Zhang, H. Sheng, Z. Wang, B. Gludovatz, Z. Zhang, E.P. George, Q. Yu, S.X. Mao, R.O. Ritchie, Dislocation mechanisms and 3D twin architectures generate exceptional strength-ductility-toughness combination in CrCoNi medium-entropy alloy, Nat. Commun. 8 (1) (2017) 14390.

[8] B. Gludovatz, A. Hohenwarter, D. Catoor, E.H. Chang, E.P. George, R.O. Ritchie, A fracture-resistant high-entropy alloy for cryogenic applications, Science 345 (6201) (2014) 1153–1158.

[9] G. Laplanche, A. Kostka, O. Horst, G. Eggeler, E. George, Microstructure evolution and critical stress for twinning in the CrMnFeCoNi high-entropy alloy, Acta Mater 118 (2016) 152–163.

[10] N.L. Okamoto, S. Fujimoto, Y. Kambara, M. Kawamura, Z.M. Chen, H. Matsunoshita, K. Tanaka, H. Inui, E.P. George, Size effect, critical resolved shear stress, stacking fault energy, and solid solution strengthening in the CrMnFeCoNi high-entropy alloy, Sci. Rep. 6 (1) (2016) 35863.

[11] S.H. Joo, H. Kato, M. Jang, J. Moon, C. Tsai, J. Yeh, H. Kim, Tensile deformation behavior and deformation twinning of an equimolar CoCrFeMnNi high-entropy alloy, Mater. Sci. Eng. A 689 (2017) 122–133.

[12] S. Yoshida, T. Bhattacharjee, Y. Bai, N. Tsuji, Friction stress and Hall-Petch relationship in CoCrNi equi-atomic medium entropy alloy processed by severe plastic deformation and subsequent annealing, Scr. Mater. 134 (2017) 33–36.

[13] H. Shahmir, J. He, Z. Lu, M. Kawasaki, T.G. Langdon, Effect of annealing on mechanical properties of a nanocrystalline CoCrFeNiMn high-entropy alloy processed by high-pressure torsion, Mater. Sci. Eng. A 676 (2016) 294–303.

[14] H. Shahmir, T. Mousavi, J. He, Z. Lu, M. Kawasaki, T.G. Langdon, Microstructure and properties of a CoCrFeNiMn high-entropy alloy processed by equal-channel angular pressing, Mater. Sci. Eng. A 705 (2017) 411–419.

[15] Y. Zhu, X. Wu, Heterostructured materials, Prog. Mater. Sci. 131 (2023) 101019.

[16] X. Wu, M. Yang, F. Yuan, G. Wu, Y. Wei, X. Huang, Y. Zhu, Heterogeneous lamella structure unites ultrafine-grain strength with coarse-grain ductility, PNAS 112 (47) (2015) 14501–14505.

[17] X. Wu, Y. Zhu, Heterogeneous materials: a new class of materials with unprecedented mechanical properties, Mater. Res. Lett. 5 (8) (2017) 527–532.

[18] Y. Zhu, X. Wu, Perspective on hetero-deformation induced (HDI) hardening and back stress, Mater. Res. Lett. 7 (10) (2019) 393–398.

[19] Y. Wang, Y. Zhu, Z. Yu, J. Zhao, Y. Wei, Hetero-zone boundary affected region: a primary microstructural factor controlling extra work hardening in heterostructure, Acta Mater 241 (2022) 118395.

[20] Y. Wang, M. Chen, F. Zhou, E. Ma, High tensile ductility in a nanostructured metal, Nature 419 (6910) (2002) 912–915.

[21] P. Sathiyamoorthi, H.S. Kim, High-entropy alloys with heterogeneous microstructure: processing and mechanical properties, Prog. Mater. Sci. 123 (2022) 100709.

[22] M. Yang, D. Yan, F. Yuan, P. Jiang, E. Ma, X. Wu, Dynamically reinforced heterogeneous grain structure prolongs ductility in a medium-entropy alloy with gigapascal yield strength, PNAS 115 (28) (2018) 7224–7229.

[23] S. Wu, G. Wang, Q. Wang, Y. Jia, J. Yi, Q. Zhai, J. Liu, B. Sun, H. Chu, J. Shen, Enhancement of strength-ductility trade-off in a high-entropy alloy through a heterogeneous structure, Acta Mater 165 (2019) 444–458.

[24] C. Slone, J. Miao, E.P. George, M.J. Mills, Achieving ultra-high strength and ductility in equiatomic CrCoNi with partially recrystallized microstructures, Acta Mater 165 (2019) 496–507.

[25] J. Su, D. Raabe, Z. Li, Hierarchical microstructure design to tune the mechanical behavior of an interstitial TRIP-TWIP high-entropy alloy, Acta Mater 163 (2019) 40–54.

[26] Q. Pan, L. Zhang, R. Feng, Q. Lu, K. An, A.C. Chuang, J.D. Poplawsky, P.K. Liaw, L. Lu, Gradient cell–structured high-entropy alloy with exceptional strength and ductility, Science 374 (6570) (2021) 984–989.

[27] X. Du, W. Li, H. Chang, T. Yang, G. Duan, B. Wu, J. Huang, F. Chen, C. Liu, W. Chuang, Dual heterogeneous structures lead to ultrahigh strength and uniform ductility in a Co-Cr-Ni medium-entropy alloy, Nat. Commun. 11 (1) (2020) 2390.

[28] P. Shi, Y. Zhong, Y. Li, W. Ren, T. Zheng, Z. Shen, B. Yang, J. Peng, P. Hu, Y. Zhang, Multistage work hardening assisted by multi-type twinning in ultrafine-grained heterostructural eutectic high-entropy alloys, Mater. Today 41 (2020) 62–71.

[29] P. Shi, W. Ren, T. Zheng, Z. Ren, X. Hou, J. Peng, P. Hu, Y. Gao, Y. Zhong, P. K. Liaw, Enhanced strength–ductility synergy in ultrafine-grained eutectic high-entropy alloys by inheriting microstructural lamellae, Nat. Commun. 10 (1) (2019) 489.

[30] C.J. Tong, Y.L. Chen, J.W. Yeh, S.J. Lin, S.K. Chen, T.T. Shun, C.H. Tsau, S. Y. Chang, Microstructure characterization of AlxCoCrCuFeNi high-entropy alloy system with multiprincipal elements, Metall. Mater. Trans. A 36 (2005) 881–893.

[31] Y. Lu, X. Gao, L. Jiang, Z. Chen, T. Wang, J. Jie, H. Kang, Y. Zhang, S. Guo, H. Ruan, Directly cast bulk eutectic and near-eutectic high entropy alloys with balanced strength and ductility in a wide temperature range, Acta Mater 124 (2017) 143–150.

[32] Y. Lu, Y. Dong, S. Guo, L. Jiang, H. Kang, T. Wang, B. Wen, Z. Wang, J. Jie, Z. Cao, A promising new class of high-temperature alloys: eutectic high-entropy alloys, Sci. Rep. 4 (1) (2014) 6200.

[33] M. Lucas, G. Wilks, L. Mauger, J.A. Munoz, O.N. Senkov, E. Michel, J. Horwath, S. Semiatin, M.B. Stone, D.L. Abernathy, Absence of long-range chemical ordering in equimolar FeCoCrNi, Appl. Phys. Lett. 100 (25) (2012).

[34] Q. Lin, J. Liu, X. An, H. Wang, Y. Zhang, X. Liao, Cryogenic-deformation-induced phase transformation in an FeCoCrNi high-entropy alloy, Mater. Res. Lett. 6 (4) (2018) 236–243.

[35] T. Zhang, S. Ma, D. Zhao, Y. Wu, Y. Zhang, Z. Wang, J. Qiao, Simultaneous enhancement of strength and ductility in a NiCoCrFe high-entropy alloy upon dynamic tension: micromechanism and constitutive modeling, Int. J. Plast. 124 (2020) 226–246.

[36] M.H. Tsai, A.C. Fan, H.A. Wang, Effect of atomic size difference on the type of major intermetallic phase in arc-melted CoCrFeNiX high-entropy alloys, J. Alloys Compd. 695 (2017) 1479–1487.

[37] J.H. Li, T. Chang, Z.C. Wu, M.H. Tsai, Quantitative prediction of solid solubility limit in single phase high-entropy alloys, Appl. Phys. Lett. 119 (14) (2021).

[38] J.H. Li, M.H. Tsai, Theories for predicting simple solid solution high-entropy alloys: classification, accuracy, and important factors impacting accuracy, Scr. Mater. 188 (2020) 80–87.

[39] M.R. He, S. Wang, S. Shi, K. Jin, H. Bei, K. Yasuda, S. Matsumura, K. Higashida, I. M. Robertson, Mechanisms of radiation-induced segregation in CrFeCoNi-based single-phase concentrated solid solution alloys, Acta Mater 126 (2017) 182–193.

[40] Z.J. Chen, T. Zhang, X.Y. Gao, Y.J. Huang, X.H. Qin, Y.F. Wang, K. Zhao, X. Peng, C. Zhang, L. Liu, Engineering microdomains of oxides in high-entropy alloy electrodes toward efficient oxygen evolution, Adv. Mater. 33 (33) (2021) 2101845.

[41] K. Christofidou, E. Pickering, P. Orsatti, P. Mignanelli, T. Slater, H. Stone, N. Jones, On the influence of Mn on the phase stability of the CrMnxFeCoNi high entropy alloys, Intermetallics 92 (2018) 84–92.

[42] Z.Y. Chen, J.H. Li, S.Y. Tung, M.H. Tsai, On the phase constituents of three CoCrFeNiX (X= B, Al, Ga) high-entropy alloys after prolonged annealing, J. Alloys Compd. 900 (2022) 163388.

[43] J. He, H. Wang, Y. Wu, X. Liu, H. Mao, T. Nieh, Z. Lu, Precipitation behavior and its effects on tensile properties of FeCoNiCr high-entropy alloys, Intermetallics 79 (2016) 41–52.

[44] Y. Shi, B. Yang, X. Xie, J. Brechtl, K.A. Dahmen, P.K. Liaw, Corrosion of Al xCoCrFeNi high-entropy alloys: al-content and potential scan-rate dependent pitting behavior, Corros. Sci. 119 (2017) 33–45.

[45] A. Verma, P. Tarate, A. Abhyankar, M. Mohape, D. Gowtam, V. Deshmukh, T. Shanmugasundaram, High temperature wear in CoCrFeNiCux high entropy alloys: the role of Cu, Scr. Mater 161 (2019) 28–31.

[46] G. Laplanche, A. Kostka, C. Reinhart, J. Hunfeld, G. Eggeler, E. George, Reasons for the superior mechanical properties of medium-entropy CrCoNi compared to high-entropy CrMnFeCoNi, Acta Mater 128 (2017) 292–303.

[47] S. Liu, Y. Wu, H. Wang, J. He, J. Liu, C. Chen, X. Liu, H. Wang, Z. Lu, Stacking fault energy of face-centered-cubic high entropy alloys, Intermetallics 93 (2018) 269–273.

[48] Y. Wang, B. Liu, K. Yan, M. Wang, S. Kabra, Y.L. Chiu, D. Dye, P.D. Lee, Y. Liu, B. Cai, Probing deformation mechanisms of a FeCoCrNi high-entropy alloy at 293 and 77K using in situ neutron diffraction, Acta Mater 154 (2018) 79–89.

[49] W. Liu, J. He, H. Huang, H. Wang, Z. Lu, C. Liu, Effects of Nb additions on the microstructure and mechanical property of CoCrFeNi high-entropy alloys, Intermetallics 60 (2015) 1–8.

[50] H. Ma, C.H. Shek, Effects of Hf on the microstructure and mechanical properties of CoCrFeNi high entropy alloy, J. Alloys Compd. 827 (2020) 154159.

[51] F. Zheng, G. Zhang, X. Chen, X. Yang, Z. Yang, Y. Li, J. Li, A new strategy of tailoring strength and ductility of CoCrFeNi based high-entropy alloy, Mater. Sci. Eng. A 774 (2020) 138940.

[52] J. Wang, F. Peng, L. Zhou, Y. Luo, W. Zhang, Z. Wu, High-Strength Ductility Joining of Multicomponent Alloy to 304 Stainless Steel Using Laser Welding Technique, Materials (Basel) 16 (6) (2023) 2374.

[53] J. Li, D. Ouyang, Q. Wang, Q. Teng, C. Cai, Q. Wei, Achieving superior tensile strength of CoCrFeNiTi0.3 high-entropy alloy via in-situ laser powder bed fusion of CoCrFeNi and Ti, Mater. Sci. Eng. A 886 (2023) 145649.

[54] Z. Sun, X. Tan, C. Wang, M. Descoins, D. Mangelinck, S.B. Tor, E.A. Jägle, S. Zaefferer, D. Raabe, Reducing hot tearing by grain boundary segregation engineering in additive manufacturing: example of an AlxCoCrFeNi high-entropy alloy, Acta Mater 204 (2021) 116505.

[55] Z. Zhang, Y. Xie, X. Huo, S. Chan, J. Liang, Y. Luo, D. Mu, J. Ju, J. Sun, J. Wang, Microstructure and mechanical properties of ultrafine grained CoCrFeNi and CoCrFeNiAl0.3 high entropy alloys reinforced with Cr2O3/Al2O3 nanoparticles, Mater. Sci. Eng. A 816 (2021) 141313.

[56] W. Huo, F. Fang, H. Zhou, Z. Xie, J. Shang, J. Jiang, Remarkable strength of CoCrFeNi high-entropy alloy wires at cryogenic and elevated temperatures, Scr. Mater. 141 (2017) 125–128.

[57] M. Yang, Y. Pan, F. Yuan, Y. Zhu, X. Wu, Back stress strengthening and strain hardening in gradient structure, Mater. Res. Lett. 4 (3) (2016) 145–151.

[58] Y. Cao, S. Ni, X. Liao, M. Song, Y. Zhu, Structural evolutions of metallic materials processed by severe plastic deformation, Mater. Sci. Eng. R Rep. 133 (2018) 1–59.

[59] T.B. Britton, A.J. Wilkinson, Stress fields and geometrically necessary dislocation density distributions near the head of a blocked slip band, Acta Mater 60 (16) (2012) 5773–5782.

[60] R. Armstrong, F. Zerilli, Dislocation mechanics aspects of plastic instability and shear banding, Mech. Mater. 17 (2–3) (1994) 319–327.

[61] J. Bailey, P. Hirsch, The dislocation distribution, flow stress, and stored energy in cold-worked polycrystalline silver, Philos. Mag. 5 (53) (1960) 485–497.

[62] III C. Zhu, T. Harrington, G.T. Gray, K.S. Vecchio, Dislocation-type evolution in quasi-statically compressed polycrystalline nickel, Acta Mater 155 (2018) 104–116.

[63] Y. Jin, B. Lin, A.D. Rollett, G.S. Rohrer, M. Bernacki, N. Bozzolo, Thermo-mechanical factors influencing annealing twin development in nickel during recrystallization, J. Mater. Sci. 50 (2015) 5191–5203.

[64] K. Lu, L. Lu, S. Suresh, Strengthening materials by engineering coherent internal boundaries at the nanoscale, Science 324 (5925) (2009) 349–352.

[65] Y. Jin, B. Lin, M. Bernacki, G.S. Rohrer, A. Rollett, N. Bozzolo, Annealing twin development during recrystallization and grain growth in pure nickel, Mater. Sci. Eng. A 597 (2014) 295–303.

[66] N. Bozzolo, M. Bernacki, Viewpoint on the formation and evolution of annealing twins during thermomechanical processing of FCC metals and alloys, Metall. Mater. Trans. A-Phys. Metall. Mater. Sci. 51 (2020) 2665–2684.

[67] A. Berger, P.J. Wilbrandt, F. Ernst, U. Klement, P. Haasen, On the generation of new orientations during recrystallization: recent results on the recrystallization of tensile-deformed fcc single crystals, Prog. Mater. Sci. 32 (1) (1988) 1–95.

[68] G. Laplanche, O. Horst, F. Otto, G. Eggeler, E. George, Microstructural evolution of a CoCrFeMnNi high-entropy alloy after swaging and annealing, J. Alloys Compd. 647 (2015) 548–557.

[69] Q. He, T. Huang, L. Shuai, Y. Zhang, G. Wu, X. Huang, D.J. Jensen, In-situ investigation of the evolution of annealing twins in high purity aluminium, Scr. Mater. 153 (2018) 68–72.

[70] H. Paul, J.H. Driver, C. Maurice, A. Piątkowski, Recrystallization mechanisms of low stacking fault energy metals as characterized on model silver single crystals, Acta Mater 55 (3) (2007) 833–847.

[71] L. Kaushik, J. Singh, J.H. Kang, Y.S. Ko, D.I. Kim, J.Y. Suh, S.H. Choi, Deciphering the role of multiple generations of annealing twins on texture evolution in cold-rolled high entropy alloys during annealing, Scr. Mater. 205 (2021) 114221.

[72] X.M. Chen, Y. Lin, F. Wu, EBSD study of grain growth behavior and annealing twin evolution after full recrystallization in a nickel-based superalloy, J. Alloys Compd. 724 (2017) 198–207.

[73] F. Lin, Y. Zhang, A. Godfrey, D.J. Jensen, Twinning during recrystallization and its correlation with the deformation microstructure, Scr. Mater. 219 (2022) 114852.

[74] D.L. Olmsted, S.M. Foiles, E.A. Holm, Survey of computed grain boundary properties in face-centered cubic metals: I. Grain boundary energy, Acta Mater 57 (13) (2009) 3694–3703.

[75] K.Y. Tsai, M.H. Tsai, J.W. Yeh, Sluggish diffusion in Co–Cr–Fe–Mn–Ni high-entropy alloys, Acta Mater 61 (13) (2013) 4887–4897.

[76] P. Bhattacharjee, G. Sathiaraj, M. Zaid, J. Gatti, C. Lee, C.W. Tsai, J.W. Yeh, Microstructure and texture evolution during annealing of equiatomic CoCrFeMnNi high-entropy alloy, J. Alloys Compd. 587 (2014) 544–552.

[77] Z. Wu, H. Bei, F. Otto, G.M. Pharr, E.P. George, Recovery, recrystallization, grain growth and phase stability of a family of FCC-structured multi-component equiatomic solid solution alloys, Intermetallics 46 (2014) 131–140.

[78] W. Liu, Y. Wu, J. He, T. Nieh, Z. Lu, Grain growth and the Hall–Petch relationship in a high-entropy FeCrNiCoMn alloy, Scr. Mater. 68 (7) (2013) 526–529.

[79] M.H. Tsai, C.W. Wang, C.W. Tsai, W.J. Shen, J.W. Yeh, J.Y. Gan, W.W. Wu, Thermal stability and performance of NbSiTaTiZr high-entropy alloy barrier for copper metallization, J. Electrochem. Soc. 158 (11) (2011) H1161.

[80] P.K. Huang, J.W. Yeh, Inhibition of grain coarsening up to 1000°C in (AlCrNbSiTiV) N superhard coatings, Scr. Mater. 62 (2) (2010) 105–108.

[81] E. Hall, The deformation and ageing of mild steel: III discussion of results, Proc. Phys. Soc. B 64 (9) (1951) 747.

[82] N. Petch, The cleavage strength of polycrystals, J. Iron Steel Inst. 174 (1953) 25–28.

[83] S. Yoshida, T. Ikeuchi, T. Bhattacharjee, Y. Bai, A. Shibata, N. Tsuji, Effect of elemental combination on friction stress and Hall-Petch relationship in face-centered cubic high/medium entropy alloys, Acta Mater 171 (2019) 201–215.

[84] X. Fan, R. Qu, Z. Zhang, Relation between strength and hardness of high-entropy alloys, Acta Metall. Sin. (Engl. Lett.) 34 (11) (2021) 1461–1482.

[85] X. Dong, Y. Shen, Y. Zhu, Moderating strain hardening rate to produce high ductility and high strength in a medium carbon TRIP steel, Mater. Res. Lett. 11 (1) (2023) 69–75.

[86] Y. Wang, C. Huang, X. Ma, J. Zhao, F. Guo, X. Fang, Y. Zhu, Y. Wei, The optimum grain size for strength-ductility combination in metals, Int. J. Plast. 164 (2023) 103574.

[87] M. Lucas, L. Mauger, J. Munoz, Y. Xiao, A. Sheets, S. Semiatin, J. Horwath, Z. Turgut, Magnetic and vibrational properties of high-entropy alloys, J. Appl. Phys. 109 (7) (2011).